

## Article

# Significance of Nanoparticle Radius and Gravity Modulation on Dynamics of Nanofluid over Stretched Surface via Finite Element Simulation: The Case of Water-Based Copper Nanoparticles

Bagh Ali <sup>1,†</sup> , Anum Shafiq <sup>2</sup>, Meznah M. Alanazi <sup>3,\*</sup>, Awatif A. Hendi <sup>3</sup>, Ahmed Kadhim Hussein <sup>4</sup>  and Nehad Ali Shah <sup>5,\*</sup> 

- <sup>1</sup> School of Mechanical Engineering and Automation, Harbin Institute of Technology, Shenzhen 518055, China
- <sup>2</sup> School of Mathematics and Statistics, Nanjing University of Information Science and Technology, Nanjing 210044, China
- <sup>3</sup> Department of Physics, College of Science, Princess Nourah bint Abdulrahman University, P.O. Box 84428, Riyadh 11671, Saudi Arabia
- <sup>4</sup> Mechanical Engineering Department, College of Engineering, University of Babylon, Hilla 00964, Iraq
- <sup>5</sup> Department of Mechanical Engineering, Sejong University, Seoul 05006, Republic of Korea
- \* Correspondence: mmalenazy@pnu.edu.sa (M.M.A.); nehadali199@sejong.ac.kr (N.A.S)
- † Bagh Ali and Nehad Ali Shah contributed equally to this work and are co-first authors.

**Abstract:** This communication studies the importance of varying the radius  $D_p$  of Copper nanoparticles for microgravity-modulated mixed convection in micropolar nanofluid flux under an inclined surface subject magnetic field and heat source. In the current era, extremely pervasive modernized technical implementations have drawn attention to free convection governed by g-jitter force connected with microgravity. Therefore, fixed inter-spacing of nanoparticles and effects of g-jitter on the inclined surface are taken into consideration. A mathematical formulation based on conservation principles was non-dimensionalized by enforcement of similarity transformation, yielding a related set of ODEs. The convective non-linearity and coupling, an FE discretization, was implemented and executed on the Matlab platform. The numerical process' credibility was ensured for its acceptable adoption with the defined outcomes. Then, the computational endeavor was continued to elucidate the impacts of various inputs of  $D_p$ , the amplitude of modulation  $\epsilon$ , material parameter  $\beta$ , mixed convection parameter  $\lambda$ , inclination angle  $\gamma$ , and magnetic parameter  $M$ . The enlarging size of nanoparticles accelerated the nanofluid flow due to the depreciation of viscosity and receded the fluid temperature by reducing the surface area for heat transportation. The modulated Nusselt number, couple stress, and skin friction coefficient are significantly affected by the variation of  $D_p$ ,  $M$ ,  $\beta$ ,  $\lambda$ , and  $\epsilon$ . These results would benefit experts dealing with upper space transportation and materials' performance, such as the effectualness of chemical catalytic reactors and crystals.

**Keywords:** finite element method; gravity modulation; micropolar fluid; nanoparticle radius; MHD

**MSC:** 5Q30; 76D05; 76R10



**Citation:** Ali, B.; Shafiq, A.; Alanaz, M.M.; Hendi, A.A.; Hussein, A.K.; Shah, N.A. Significance of Nanoparticle Radius and Gravity Modulation on Dynamics of Nanofluid over Stretched Surface via Finite Element Simulation: The Case of Water-Based Copper Nanoparticles. *Mathematics* **2023**, *11*, 1266. <https://doi.org/10.3390/math11051266>

Academic Editors: Nikolay M. Zubarev and Evgeny A. Kochurin

Received: 5 January 2023

Revised: 13 February 2023

Accepted: 17 February 2023

Published: 6 March 2023



**Copyright:** © 2023 by the authors. Licensee MDPI, Basel, Switzerland. This article is an open access article distributed under the terms and conditions of the Creative Commons Attribution (CC BY) license (<https://creativecommons.org/licenses/by/4.0/>).

## 1. Introduction

Increasing the heat conduction capacity of nanofluids is a significant concern of modern-day research experts. The improvement in heat conduction capability depends upon the base fluid's nature and the different parameters of nanoparticles. Other physical parameters remain under discussion for researchers, such as the concentration of nano-sized particles, viscosity, and temperature effect due to different mass-to-density ratios [1,2]. Wei et al. [3] inquired about the impacts of size and thickness on the number, surface zone,

hardening productivity, and explicit surface zone of nanoparticles in polymer nanocomposites. They found that dust and nano-sized particles are responsible for enhanced thermal performance, Goodarzi et al. [4] studied the experimental dynamics of MWCNTs-ZnO/engine oil and hybrid nanolubricants that are based on variations in heat and concentration and found that nanofluid viscosity shows a decline against raising the heat at a constant fraction of volume. Zadeh et al. [5] examined the nanofluid dynamic viscosity through experiments and resulted that the fluid's dynamic viscosity reduces with enhancement in heat. Hamid et al. [6] analyzed the effect of nanoparticles shapes of Molybdenum disulfide ( $\text{MoS}_2$ ) on the rotating flux of nanoliquid with thermal radiations and magnetic effect above a flexible extended sheet. Yapici et al. [7] studied the impact of different metallic oxide nanoparticle concentration and size upon the rheology of base nanofluid, specifically ethylene glycol. Gajghate et al. [8] experimentally examined the impact of Zirconia nanoparticles and analyzed the heat transportation with deionized water subject to stability, turbulence, and viscosity tests, affirming a superior scattering of nanoparticles. Shah et al. [9] explored the importance of an increase in the radius of nanoparticles, Soret, and Dufour effects for the fluid dynamics under the magnetic influence. Attention has been given to the flows of nanofluids under different physical configurations [10–14].

Due to the wide variety of physical designs, analysis of non-Newtonian fluids has attained enormous interest in various zones of engineering, biomedical engineering, and industrial and technical implementations. For example, blood, shampoo, oils, paints, drilling mud, and ketchup are non-Newtonian fluids. Micropolar liquid indicates the micromovements of components of fluid and microscopic influences resulting from a local structure. The micropolar fluids theory, illustrating both the microinertia effect and micro rotation, was suggested by Eringen [15,16]. Further, Wilson [17] rendered the idea of approximating the boundary layer in micropolar fluids towards surfaces. By ignoring specific microinertia terminology and utilizing the reasoning of order-of-magnitude, he acquired adequate two-dimensional boundary layer systems. A few articles have been written about the issues of micropolar fluids' boundary layer flux [18–20].

The semiconductor industry has highlighted the magnetic field's usage to monitor melt motion during single crystal fabrication. The influence of magnetic damping stems from various sources including microgravity, which reduces the g-jitter impact subject to an appropriate magnetic field [21]. Baumgartl, Ma, and Walker [22], as well as Muller [23,24], investigated g-jitter-driven melt flux associated with the experiments on the development of space crystal. Li and his colleague [25,26] documented a wide range of studies involving computational simulation and theoretical magnetic field applications on mass transport and g-jitter-driven flows. Many other researchers used actual g-jitter data and simulated g-jitter signatures from regular space flights to better understand heat and flow phenomena in a real-world g-jitter environment.

For g-jitter theoretical studies, a mathematical model was built that is appropriate within a spaceport for various materials science investigations. Several researchers explored g-jitters speculative fluid activity on the fluid flow of the boundary layer (see [27,28]). This research aids in the preparation of fundamental experimental analysis for non-Newtonian and Newtonian fluids using g-jitter. The gravity modulation impact by magnetic convection in fluids with angular momentum produced internally was investigated using g-jitter-induced viscous fluid [29]. In addition, studies have also been carried out on the impact of modulation of periodic gravity produced by heat transmission features and mixed convective flux with a vertically stretching surface in incompressible and viscous liquids [30]. Moreover, the importance of gravity modulation in conjunction with Darcy convection at the vertical flux was also explored by [31].

The abovementioned analysis suggest that nanoliquids are a potential channel for enlarged heat transmission because of their productive thermal attributes such as the ratio of mass to density, thermal conductivity, and specific heat capacity. However, these days, research interest has diverted to analyzing the role of the radius of nanoparticles and spacing between them. The change in nanoparticle radius impacts the characteristics of

nanoparticles and interphase [32], and also influences the nature of energy transfer between the surface of nanoparticles and fluid’s layers [33]. Motivated by such an indispensable notion, this work is undertaken to elaborate on the impact of nanoparticle radius for g-jitter mixed convection of nanofluid transportation due to an inclined surface. The present report results may be beneficial in the thermal fluids designed for material processing in space. In this scenario, the current elaborated fluid model answers the following research questions:

- How does the radius of nanoparticles influence the transport phenomena of Cu-nanofluids in micro gravity environment?
- What role does the variable radius of nanoparticles have in the decreased and regulated factor of skin friction, thermal transfer rate, and couple stress at the inclined surface?
- What is the role of modulation amplitude and oscillation frequency on fluid dynamics with mixed convection due to the inclined and expanding surface in microgravity environments?

Finite element discretization is utilized to attain numerical solution of the non-linear coupled formulation, because it solve various boundary value problems related to fluid dynamics very rapidly, adequately, and precisely [34,35].

### 2. Mathematical Formulation

We assume that microgravity impacts the flux of non-Newtonian liquids and attributes of the temperature of Cu/H<sub>2</sub>O (nanofluids) due to an expanding inclined surface (plate), as in Figure 1.  $T_\infty$ ,  $T_w$ ,  $B_0$ , and  $\gamma$  are ambient temperature, constant temperature, uniformly magnetic strength in the y-direction, and acute angle, respectively. Further, in the x-direction, the plate is extending, and the y-axis is perpendicular to the plate’s surface. It is supposed that linear velocity is  $u_w = bx$ , where ( $b > 0$ ). The thermophysical characteristics of H<sub>2</sub>O and Cu solid particles are displayed in Tables 1 and 2. The aggregation of tiny particles is neglected because the nanofluid’s mixture is assumed to be a stable compound. Further, the gravitational field  $g^*(t) = [g_0 + g_0a \cos(\pi\omega t)]$  is incorporated in the momentum equation [36]. Here,  $g^*(t)$  and  $g_0$  denote the acceleration time-averaged value due to  $K$  unit vector; gravity is in an upward direction; and  $t$ ,  $\omega$ , and  $a$  are time, oscillation frequency, and scaling parameter, respectively. Under the aforementioned factors, the problem’s governing equations are the following [37,38]:

$$\partial_x \tilde{u}_1 + \partial_y \tilde{u}_2 = 0, \tag{1}$$

$$\rho_{n_f}(\partial_t \tilde{u}_1 + \tilde{u}_1 \partial_x \tilde{u}_1 + \tilde{u}_2 \partial_y \tilde{u}_1) = (\mu_{n_f} + \kappa) \partial_{yy} \tilde{u}_1 - \sigma B_0^2 \mu_1 + \kappa \partial_y \tilde{N} + g^*(t)(\tilde{T} - \tilde{T}_\infty)(\rho\beta) \cos \gamma, \tag{2}$$

$$\rho j(\partial_t \tilde{N} + \tilde{u}_1 \partial_x \tilde{N} + \tilde{u}_2 \partial_y \tilde{N}) = \gamma^*(\mu_f + \frac{\kappa}{2}) \partial_{yy} \tilde{N} - \kappa(2N + \partial_x \tilde{u}_1), \tag{3}$$

$$\partial_t \tilde{T} + \tilde{u}_1 \partial_x \tilde{T} + \tilde{u}_2 \partial_y \tilde{T} = \tilde{\alpha} \partial_{yy} \tilde{T} + \frac{Q_0}{\rho C_p} (\tilde{T} - \tilde{T}_\infty). \tag{4}$$

The related boundary conditions are

$$\left. \begin{aligned} t = 0 : \tilde{u}_1 = \tilde{u}_2 = 0, \tilde{T} = \tilde{T}_\infty, \\ t > 0 : \tilde{u}_1 = \tilde{u}_w, \tilde{u}_2 = 0, \tilde{N} = 0, \tilde{T} = \tilde{T}_w, \text{ as } y = 0, \\ \tilde{u}_1 \rightarrow 0, \tilde{T} \rightarrow \tilde{T}_\infty, \tilde{N} \rightarrow 0, \text{ as } y \rightarrow \infty. \end{aligned} \right\} \tag{5}$$

Above,  $\tilde{u}_1$  and  $\tilde{u}_2$  are velocity components in the x and y directions;  $\tilde{T}$ ,  $\sigma$ ,  $\mu_{n_f}$ ,  $\tilde{N}$ ,  $\tilde{\alpha}$ ,  $\rho_{n_f}$ , and  $\gamma^*$  are temperature of fluid, electrical conductivity, dynamic viscosity, angular velocity, thermal diffusion, density, and spin gradient viscosity, respectively. Now, we use the below similarity transformations (see [37,39]):

$$\eta = \sqrt{\frac{\tilde{b}y^2}{\nu}}, \Gamma = \tilde{b}t, N = \sqrt{\frac{\tilde{b}}{\nu}} H(\tau, \eta), \psi = \sqrt{\tilde{b}\nu} x F(\tau, \eta), \theta(\tau, \eta) = \frac{\tilde{T} - \tilde{T}_\infty}{\tilde{T}_w - \tilde{T}_\infty}, \tau = b\omega. \tag{6}$$

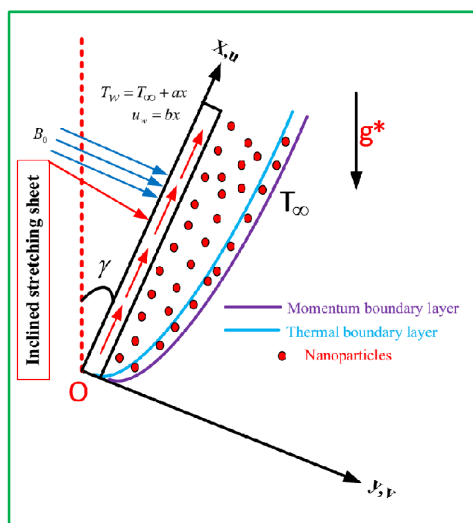


Figure 1. Geometry of model.

Table 1. Thermophysical characteristics of water-based fluid and nanoparticles [40,41].

Physical Properties	$\rho$ (kg m <sup>-3</sup> )	$C_p$ (J kg <sup>-1</sup> K <sup>-1</sup> )	$\kappa$ (Wm <sup>-1</sup> K <sup>-1</sup> )	$\beta \times 10^5$ (K <sup>-1</sup> )
H <sub>2</sub> O	0991.1	4179.0	00.613	21.000
Cu	8933.0	0385.0	0401.0	1.6700

Table 2. Thermophysical attributes of base fluid and nanoparticles [40–43].

Properties	Nanofluid
Viscosity ( $\mu$ )	$\frac{\mu_{nf}}{\mu_b} = 1 + 2.5\Phi + 4.5 \left[ \frac{1}{\frac{h}{D_p} (2 + \frac{h}{D_p}) (1 + \frac{h}{D_p})^2} \right]$
Density ( $\rho$ )	$\rho_{nf} = \rho_f(1 - \Phi) + \Phi\rho_s$
Heat capacity ( $\rho C_p$ )	$(\rho C_p)_{nf} = (\rho C_p)_f(1 - \Phi) + \Phi \frac{(\rho C_p)_s}{(\rho C_p)_f}$
Thermal conductivity (k)	$\frac{k_{nf}}{k_f} = \frac{k_s + 2k_f - 2\Phi(k_f - k_s)}{k_s + 2k_f + \Phi(k_f - k_s)}$
Electrical conductivity ( $\sigma$ )	$\frac{\sigma_{nf}}{\sigma_f} = \left[ 1 + \frac{3 \left( \frac{\sigma_s}{\sigma_f} - 1 \right) \Phi}{\left( \frac{\sigma_s}{\sigma_f} + 2 \right) - \left( \frac{\sigma_s}{\sigma_f} - 1 \right) \Phi} \right]$
Coefficient of thermal expansion ( $\beta^*$ )	$(\rho\beta^*)_{nf} = (\rho\beta^*)_f(1 - \Phi) + \Phi \frac{(\rho\beta^*)_s}{(\rho\beta^*)_f}$

In Table 2,  $h$ ;  $D_p$ ; and the subscripts  $f, s$ , and  $n_f$  represent inter-particle space, radius of nanoparticles, and tiny particles of Cu and nanoliquid, respectively. Substituting Equation (6) into Equations (1)–(5) reduces to the following system of a non-linear set of non-linear PDEs:

$$\left(\frac{\chi_1}{\chi_2} + \beta\right)F''' + FF'' - \frac{M\chi_4}{\chi_2}F' - F'^2 + \frac{\chi_3\lambda}{\chi_2}\theta \cos(\gamma) + \frac{\chi_3\lambda}{\chi_2}\theta \cos(\gamma)a \cos(\pi\tau)\theta + \frac{\beta}{\chi_2}H' = \Omega \frac{\partial F'}{\partial \tau}, \tag{7}$$

$$\left(\frac{\chi_1}{\chi_2} + 0.5\beta\right)H'' + FG' - F'H - \frac{\beta}{\chi_2}(2H + F'') = \Omega \frac{\partial H}{\partial \tau}, \tag{8}$$

$$\frac{\chi_5}{\chi_6}\theta'' + PrF\theta' - PrF'\theta + \frac{Q_s}{\chi_6}\theta = Pr\Omega \frac{\partial \theta}{\partial \tau}, \tag{9}$$

$$\left. \begin{aligned} H(\tau, \eta = 0) = 0, F(\tau, \eta = 0) = 0, F'(\tau, \eta = 0) = \theta(\tau, \eta = 0) = 1, \text{ at } \eta = 0, \\ F'(\tau, \eta) \rightarrow 0, \theta(\tau, \eta) \rightarrow 0, H(\tau, \eta) \rightarrow 0, \text{ as } \eta \rightarrow \infty, \end{aligned} \right\} \tag{10}$$

where

$$\chi_1 = 1 + 2.5\Phi + 4.5 \left[ \frac{1}{\frac{h}{D_p} (2 + \frac{h}{D_p}) (1 + \frac{h}{D_p})^2} \right], \chi_2 = (1 - \Phi) + \Phi \frac{\rho_s}{\rho_f}, \chi_3 = (1 - \Phi) + \Phi \frac{(\rho\beta)_s}{(\rho\beta)_f},$$

$$\chi_4 = \left[ 1 + \frac{3(\frac{\sigma_s}{\sigma_f} - 1)\Phi}{(\frac{\sigma_s}{\sigma_f} + 2) - (\frac{\sigma_s}{\sigma_f} - 1)\Phi} \right], \chi_5 = \frac{k_s + 2k_f - 2\Phi(k_f - k_s)}{k_s + 2k_f + \Phi(k_f - k_s)}, \chi_6 = (1 - \Phi) + \Phi \frac{(\rho C_p)_s}{(\rho C_p)_f}.$$

The material parameter, Hartmann number, non-dimensional frequency, Prandtl number, mixed convection, and heat source are defined as

$$\beta = \frac{\kappa}{\mu_f}, M = \frac{\sigma B_0^2}{b\rho}, \Omega = \frac{\omega}{b}, Pr = \frac{\nu}{\alpha}, \lambda = \frac{g_0\beta(\tilde{T}_w - \tilde{T}_\infty)x^3/\nu^2}{(u_w x/\nu)^2}, Q_s = \frac{Q_0}{b\rho C_p}.$$

Skin friction coefficient and local Nusselt number expressions are described as

$$C_f = \frac{2\tau_w}{\rho u_w^2}, Nu = \frac{xq_w}{\kappa(\tilde{T}_w - \tilde{T}_\infty)}. \tag{11}$$

Here, the tensor of skin friction  $\tau_w = ((\mu_{nf} + \kappa)\partial_y \tilde{u}_1 + \kappa N)_{y=0}$ —and at the surface, heat flux—are  $q_w = -\kappa(\partial_y \tilde{T})_{y=0}$ . By Equation (6), we obtain

$$\left\{ C_{fx} Re_x^{1/2} = \left(\frac{\chi_1}{\chi_2} + K\right)F''(\tau, 0), Nu_x Re_x^{-1/2} = -\chi_5\theta(\tau, 0). \right. \tag{12}$$

*Numerical Procedure*

The FE method is noteworthy for solving several types of differentiated equations. Continuous piecewise approximation is used to reduce the error size [44]. The basic steps and outstanding detail of this strategy were sketched out by Reddy [45] and Jyothi [46]. Because of its precision and simplicity, scientists and experts have described this technique as a particularly productive instrument for examining complex technical challenges [47,48]. For solving Equations (7)–(9) with boundary condition (10), we assume first:

$$F' = \Lambda, \tag{13}$$

In view of Equation (13), Equations (7)–(10) are converted to Equations (14)–(17) and are given as follows:

$$\left(\frac{\chi_1}{\chi_2} + K\right)\Lambda'' - \Lambda^2 + F\Lambda' - \frac{M\chi_4}{\chi_2}\Lambda + \frac{\chi_3\lambda}{\chi_2}(1 + a \cos(\pi\tau))\theta \cos(\gamma) + \frac{K}{\chi_2}G' = \Omega \frac{\partial\Lambda}{\partial\tau}, \tag{14}$$

$$\left(\frac{\chi_1}{\chi_2} + \frac{K}{2}\right)G'' + FG' - \Lambda G - \frac{K}{\chi_2}(2G + \Lambda') = \Omega \frac{\partial G}{\partial\tau}, \tag{15}$$

$$\frac{\chi_5}{\chi_6}\theta'' + PrF\theta' - Pr\Lambda\theta + \frac{Q_s}{\chi_6}Pr\theta = Pr\Omega \frac{\partial\theta}{\partial\tau}, \tag{16}$$

$$\left. \begin{aligned} \Lambda(\tau, \eta = 0) = 1, F(\tau, \eta = 0) = 0, G(\tau, \eta = 0) = 0, \theta(\tau, \eta = 0) = 1, \text{ at } \eta = 0, \\ \Lambda(\tau, \eta) \rightarrow 0, G(\tau, \eta) \rightarrow 0, \theta(\tau, \eta) \rightarrow 0, \text{ as } \eta \rightarrow \infty. \end{aligned} \right\} \tag{17}$$

For numerical computation, length of the plate is fixed at  $\tau = 2.0$  and thickness of the boundary layer at  $\eta = 5.0$ . The variational forms of Equations (13)–(17) are given below:

$$\int_{\Omega_e^*} \beta_1 \{F' - \Lambda\} d\Omega_e^* = 0, \tag{18}$$

$$\int_{\Omega_e^*} \beta_2 \left\{ \left(\frac{\chi_1}{\chi_2} + K\right)\Lambda'' + F\Lambda' - \Lambda^2 - \frac{M\chi_4}{\chi_2}\Lambda + \frac{\chi_3\lambda}{\chi_2}(1 + a \cos \pi\tau)\theta \cos \gamma + \frac{K}{\chi_2}G' - \Omega \frac{\partial\Lambda}{\partial\tau} \right\} d\Omega_e^* = 0, \tag{19}$$

$$\int_{\Omega_e^*} \beta_3 \left\{ \left( \frac{\chi_1}{\chi_2} + \frac{K}{2} \right) G'' + FG' - \Lambda G - \frac{K}{\chi_2} (2G + \Lambda') - \Omega \frac{\partial G}{\partial \tau} \right\} d\Omega_e^* = 0, \tag{20}$$

$$\int_{\Omega_e^*} \beta_4 \left\{ \frac{\chi_5}{\chi_6} \theta'' + PrF\theta' - Pr\Lambda\theta + \frac{Q_s}{\chi_6} Pr\theta - Pr\Omega \frac{\partial \theta}{\partial \tau} \right\} d\Omega_e^* = 0. \tag{21}$$

Here, test functions are  $\beta_1, \beta_2, \beta_3,$  and  $\beta_4$ . Let us divide the domain ( $\Omega_e^*$ ) into four noded-elements. The associate approximations of finite-element are

$$F = \sum_{j=1}^4 F_j \Psi_j(\tau, \eta), \quad \zeta = \sum_{j=1}^4 \zeta_j \Psi_j(\tau, \eta), \quad \theta = \sum_{j=1}^4 \theta_j \Psi_j(\tau, \eta). \tag{22}$$

Here,  $\Psi_j$  ( $j = 1,2,3,4$ ) are the linear-interpolation functions for  $\Omega_e^*$  given by

$$\begin{aligned} \Psi_1 &= \frac{(\tau_{e+1} - \tau)(\eta_{e+1} - \eta)}{(\tau_{e+1} - \tau_e)(\eta_{e+1} - \eta_e)}, & \Psi_2 &= \frac{(\tau - \tau_e)(\eta_{e+1} - \eta)}{(\tau_{e+1} - \tau_e)(\eta_{e+1} - \eta_e)}, \\ \Psi_3 &= \frac{(\tau - \tau_e)(\eta - \eta_e)}{(\tau_{e+1} - \tau_e)(\eta_{e+1} - \eta_e)}, & \Psi_4 &= \frac{(\tau_{e+1} - \tau)(\eta - \eta_e)}{(\tau_{e+1} - \tau_e)(\eta_{e+1} - \eta_e)}. \end{aligned} \tag{23}$$

The developed model of finite elements of the equations is given by

$$\begin{bmatrix} [L^{11}] & [L^{12}] & [L^{13}] & [L^{14}] \\ [L^{21}] & [L^{22}] & [L^{23}] & [L^{24}] \\ [L^{31}] & [L^{32}] & [L^{33}] & [L^{34}] \\ [L^{41}] & [L^{42}] & [L^{43}] & [L^{44}] \end{bmatrix} \begin{bmatrix} \{f\} \\ \{\zeta\} \\ \{g\} \\ \{\theta\} \end{bmatrix} = \begin{bmatrix} \{r_1\} \\ \{r_2\} \\ \{r_3\} \\ \{r_4\} \end{bmatrix} \tag{24}$$

where  $[L_{mn}]$  and  $[r_m]$  ( $m,n = 1,2,3,4$ ) are defined as follows:

$$\begin{aligned} L_{ij}^{11} &= \int_{\Omega_e^*} \Psi_i \frac{d\Psi_j}{d\eta} d\Omega_e, L_{ij}^{12} = - \int_{\Omega_e} \Psi_i \Psi_j d\Omega_e^*, L_{ij}^{13} = L_{ij}^{14} = L_{ij}^{21} = L_{ij}^{31} = 0, \\ L_{ij}^{22} &= -\left(\frac{1}{\chi_1 \chi_2} + K\right) \int_{\Omega_e^*} \frac{d\Psi_i}{d\eta} \frac{d\Psi_j}{d\eta} d\Omega_e^* + \int_{\Omega_e^*} \bar{f} \Psi_i \frac{d\Psi_j}{d\eta} d\Omega_e^* - \int_{\Omega_e^*} \bar{\Lambda} \Psi_i \Psi_j d\Omega_e^* - \frac{M}{\chi_2} \int_{\Omega_e^*} \Psi_i \Psi_j d\Omega_e^* - \Omega \int_{\Omega_e^*} \Psi_i \frac{d\Psi_j}{d\tau} d\Omega_e^*, \\ L_{ij}^{23} &= \frac{K}{\chi_2} \int_{\Omega_e^*} \Psi_i \frac{d\Psi_j}{d\eta} d\Omega_e^*, L_{ij}^{24} = \frac{\chi_3 \lambda}{\chi_2} (1 + a \cos \pi \tau) \cos \gamma \int_{\Omega_e^*} \Psi_i \Psi_j d\Omega_e^*, \\ L_{ij}^{33} &= -\left(\frac{1}{\chi_1 \chi_2} + \frac{K}{2}\right) \int_{\Omega_e^*} \frac{d\Psi_i}{d\eta} \frac{d\Psi_j}{d\eta} d\Omega_e^* + \int_{\Omega_e^*} \bar{f} \Psi_i \frac{d\Psi_j}{d\eta} d\Omega_e^* - \int_{\Omega_e^*} \bar{\Lambda} \Psi_i \Psi_j d\Omega_e^* - \frac{2K}{\chi_2} \int_{\Omega_e^*} \Psi_i \Psi_j d\Omega_e^* - \Omega \int_{\Omega_e^*} \Psi_i \frac{d\Psi_j}{d\tau} d\Omega_e^*, \\ L_{ij}^{32} &= -\frac{K}{\chi_2} \int_{\Omega_e^*} \Psi_i \frac{d\Psi_j}{d\eta} d\Omega_e^*, L_{ij}^{34} = L_{ij}^{41} = L_{ij}^{42} = L_{ij}^{43} = 0, \\ L_{ij}^{44} &= -\frac{\chi_4}{\chi_5} \int_{\Omega_e^*} \frac{d\Psi_i}{d\eta} \frac{d\Psi_j}{d\eta} d\Omega_e^* + Pr \int_{\Omega_e^*} \bar{f} \Psi_i \frac{d\Psi_j}{d\eta} d\Omega_e^* - Pr \int_{\Omega_e^*} \bar{\Lambda} \Psi_i \Psi_j d\Omega_e^* - Pr\Omega \int_{\Omega_e^*} \Psi_i \frac{d\Psi_j}{d\zeta} d\Omega_e^* + Pr \frac{Q_s}{\chi_5} \int_{\Omega_e^*} \bar{\Lambda} \Psi_i \Psi_j d\Omega_e^*, \end{aligned}$$

and

$$r_i^1 = 0, r_i^2 = -\left(\frac{1}{\chi_1 \chi_2} + K\right) \oint_{\Gamma_e} \Psi_i n_\eta \frac{\partial \bar{\Lambda}}{\partial \eta} ds, r_i^3 = -\left(\frac{1}{\chi_1 \chi_2} + \frac{K}{2}\right) \oint_{\Gamma_e} \Psi_i n_\eta \frac{\partial \bar{G}}{\partial \eta} ds, r_i^4 = -\frac{\chi_4}{\chi_5} \oint_{\Gamma_e} \Psi_i n_\eta \frac{\partial \bar{\theta}}{\partial \eta} ds, \tag{25}$$

where  $\bar{F} = \sum_{j=1}^4 \bar{F}_j \Psi_j, \bar{\Lambda} = \sum_{j=1}^4 \bar{\Lambda}_j \Psi_j,$  and  $\bar{\theta}' = \sum_{j=1}^4 \bar{\theta}'_j \Psi_j$  are known. The entire domain is divided into  $101 \times 101$  rectangular units of equal size. After evaluating four functions at each node and obtaining 40804 non-linear equations after assembly, the technique of Gaussian quadrature is utilized to resolve the integration with  $10^{-5}$  accuracy.

### 3. Results and Discussion

In this segment, we demonstrate the effect of nanoparticle radius  $D_p$  on transport phenomena of fluids and heat transmission above an inclined stretching sheet affected by magnetic field and microgravity with a heat source. Two sets of curves are drawn for different inputs of  $M$  and  $\beta$  in all figures of these quantities. Further explanation is provided with the evaluation of the reduced skin friction factor  $Cf_x Re_x^{1/2}$ , local couple stress  $M_x Re_x$ , and rate of heat transfer  $Nu_x Re_x^{1/2}$  under a varied amplitude of modulation  $\epsilon$  and the radius  $D_p$ . In the analysis, the parameters default values were  $M = 2.0$ ,  $\beta = 1.0$ ,  $\lambda = 1.0$ ,  $Q_s = \epsilon = 0.2$ ,  $\gamma = \pi/6$ , and  $Pr = 0.72$ . The current technique results are compared with those of existing studies to determine their validity (see Tables 3 and 4).

Figure 2a,b reveal the enhancement in  $F'(\tau, \eta)$  (velocity) of bulk flow with enhanced radius of nanoentities  $D_p$ . The velocity curves are smooth and steadily increasing symmetrically with successive increments in  $D_p$ . This result can be elaborated in Figure 2a. For an example, corresponding to the smallest chosen value of  $D_p$  ( $D_p = 0.5$ ), the rescaled value of velocity  $F'(\tau, 1)$  is nearly 0.3, and for the highest input of  $D_p$  ( $D_p = 6.5$ ),  $F'(\tau, 1)$  is nearly 0.6. We can imagine for this situation that rescaled velocity of flow is almost doubled when the radius  $D_p$  is made thirteen times greater. This noteworthy impression of  $D_p$  on the nanofluid's transport phenomenon pertains to the lowering of the viscous effect of the fluid against the incremental size of nanoentities in conjunction with the opinions of Namburu et al. [49] and Pastoriza-Gallego et al. [50,51]. Furthermore, it is discerned that  $F'(\tau, \eta)$  lessened with increasing values of  $M$ , but slightly raised directly with material parameter  $\beta$ . The large values of  $M$  are related to a higher Lorentz force, which resists the flux. In contrast, the material parameter  $\beta$  is inversely proportional to the coefficient of dynamic viscosity; hence, its larger value means a decrement of viscous effects to make the flow faster. The graph of variation in  $H(\tau, \eta)$  with variational values of  $D_p$  in collaboration with the parameters  $M$  and  $\beta$  are sketched, respectively, in Figure 3a,b. A view of these figures suggests that with the amplified values of  $D_p$  (radius of nanoentities), the micromotion reduces close to the sheet's boundary and twists to obtain rising values far off from the sheet. In this scenario, the impression of  $D_p$  on the micromotion of the fluid particles is sizable enough to mention. In Figure 3a, the scaled peak value of microrotation is 0.08 when the elected input of  $D_p$  is the lowest ( $D_p = 0.5$ ); meanwhile, for the highest  $D_p$  ( $D_p = 6.5$ ), it obtains the highest worth less than 0.03 and close  $\eta = 1.0$ . This is because the smaller radius  $D_p$  means higher viscosity; hence, greater micromotion near the surface is generated. Further, the magnetic field strength bears little influence on micromotion, but the improved material parameter  $\beta$  places a noticeable effect on  $H(\tau, \eta)$  to be seen, respectively, in Figure 3a and 3b.

Figure 4a,b illustrate the decrement in the temperature distribution of the Cu-nanofluids when the radius  $D_p$  is enhanced in the presence of magnetic field  $M$ . This can be connected with the fact that the heat conductivity of nanofluids decreases with increasing particle size [52]. The explanation for this outcome pertains to the decreasing surface area in case of a larger size of the nanoparticles, and hence, less heat is transferred to decline the temperature curve. From Figure 4a, the growth of temperature  $\theta(\tau, \eta)$  because of rising values of  $M$  is created by slowing the motion of fluid when the kinetic energy is dissipated to thermal energy. Moreover, Figure 4b exhibits the decrement in the temperature field due to more significant inputs of material parameter  $\beta$ . The two sub-figures in Figure 5a,b in their respective order reveal that for a fixed heat source strength ( $Q_s > 0$ ) and heat sink ( $Q_s < 0$ ), the fluid temperature reduced significantly against the developing values of  $D_p$ —the nanoparticle radius. Physically, the larger nanoparticles receded the surface area for less heat transportation. Thus, the nanofluid temperature is at a higher level for smaller particles. In addition, in the presence of heat source  $Q_s$  ( $Q_s > 0$ ), the temperature increases, and it decreases when the heat sink's strength  $Q_s$  ( $Q_s < 0$ ) grows.

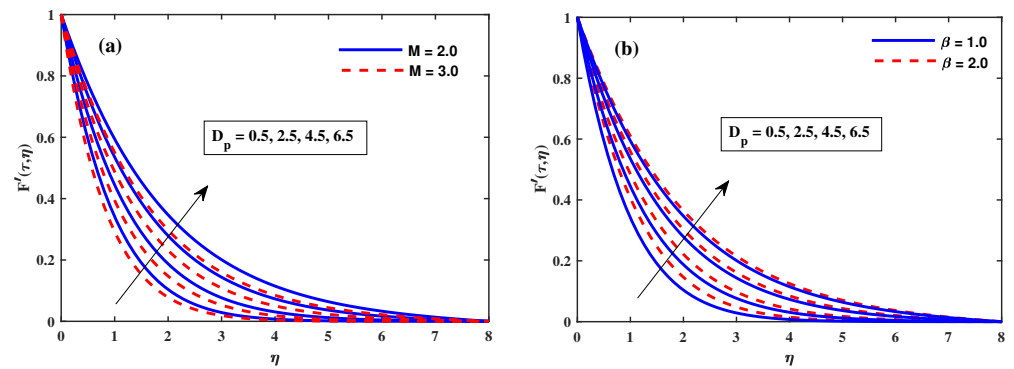


Figure 2. Curve of  $F'(\tau, \eta)$  against  $D_p$  (nanoparticle radius),  $M$  (a), and  $\beta$  (b).

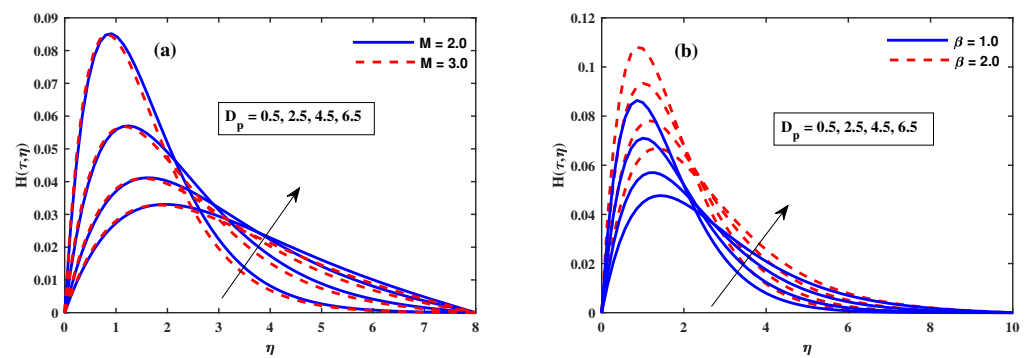


Figure 3. Curve of  $H(\tau, \eta)$  against  $D_p$  (nanoparticle radius),  $M$  (a), and  $\beta$  (b).

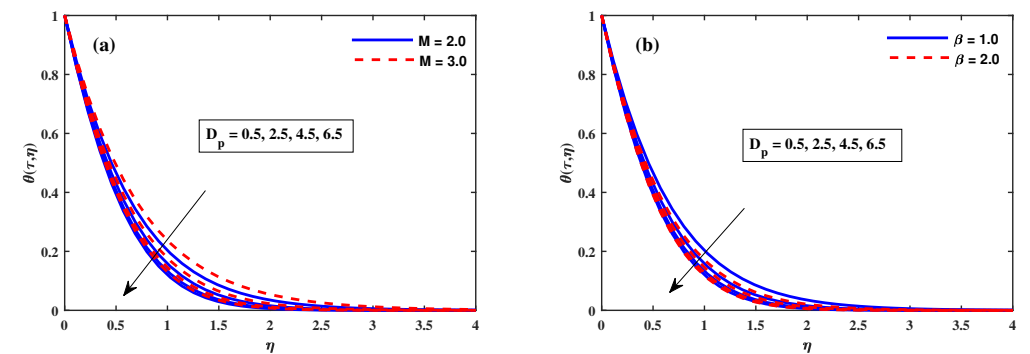


Figure 4. Curve of  $\theta(\tau, \eta)$  against  $D_p$  (nanoparticle radius), (a)  $M$  (magnetic field), and (b)  $\beta$  (material parameter).

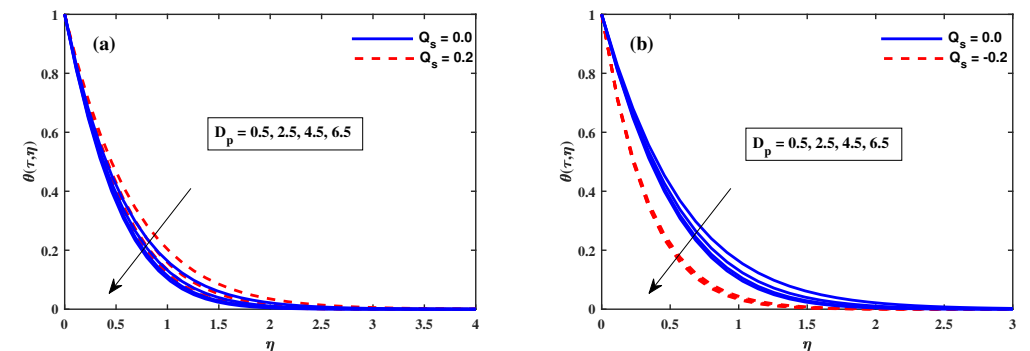


Figure 5. Curve of  $\theta(\tau, \eta)$  against (a)  $D_p$  (nanoparticle radius) and (b)  $Q_s$  (Heat source/sink).

The oscillating value of  $Cf_x Re_x^{1/2}$  ameliorates along  $\epsilon$  ( $0 \leq \epsilon \leq 1$ ) and attains lower peaks at  $\tau = 1.0$ . A differentiated result for the varying radius  $D_p$  of nanoparticles to influence the fluctuating reduced skin friction  $Cf_x Re_x^{1/2}$  is illustrated in Figure 6a. The magnitude of the skin friction factor in this situation is reduced against the enlarging values of  $D_p$ . The growing magnetic strength corresponds to a strong magnetic field, which enhances the Lorentz force. The opposing nature of Lorentz force is potently exhibited in this elaborated fluid problem, where it slowed down the fluid velocity and enhanced the magnitude of  $Cf_x Re_x^{1/2}$ . Figure 6b discloses the magnification in the modulated behavior of  $Cf_x Re_x^{1/2}$  with an improving strength of  $\beta$  in the presence of a microgravity environment. Physically, this phenomenon shows because the material parameter ( $\beta$ ) provides the resistance in fluid flow motion along the wall. From Figure 7a, the skin friction's magnitude is reduced with the growing values of  $D_p$ . Figure 7b discloses the increase in the modulated behavior of  $Cf_x Re_x^{1/2}$  with ameliorating strength of heat source parameter  $Q_s$  in the presence of environs of microgravity. Figure 8a and Figure 8b, respectively, present the pronounced fluctuation of  $Cf_x Re_x^{1/2}$  with enhancing values of mixed convection parameter  $\lambda$  and inclination angle  $\gamma$  in the presence of g-jitter effects. The modulated skin friction shows larger fluctuations for improved mixed convection and smaller inclination of the sheet. Physically, this behavior occurs because the buoyancy force decreases as the plate is inclined away from the vertical. The influence of nanoparticle radius  $D_p$  on couple stress  $M_x Re_x$  is described through delineation of Figure 9. It is noticed that increments in  $D_p$  enhance the couple stress. The quantity  $M_x Re_x$  upsurges with the developing values of parameters  $M$  and  $\beta$ .

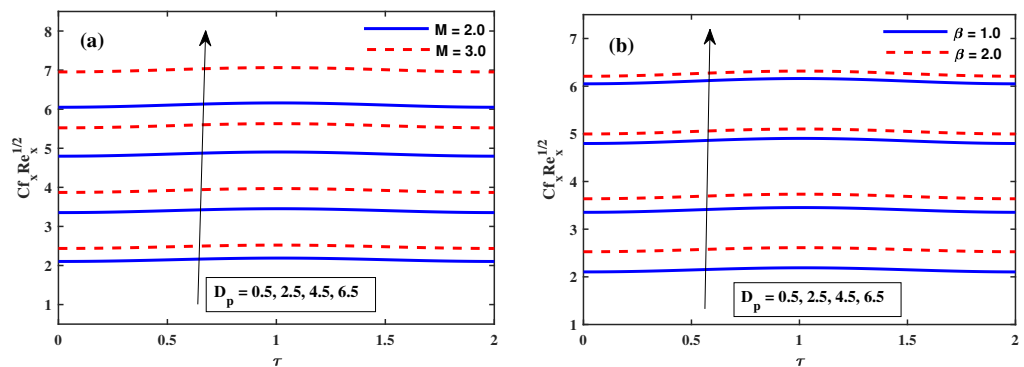


Figure 6. Fluctuation of  $Cf_x Re_x^{1/2}$  against  $D_p$  (nanoparticle radius), (a)  $M$  (magnetic field), and (b)  $\beta$  (material parameter).

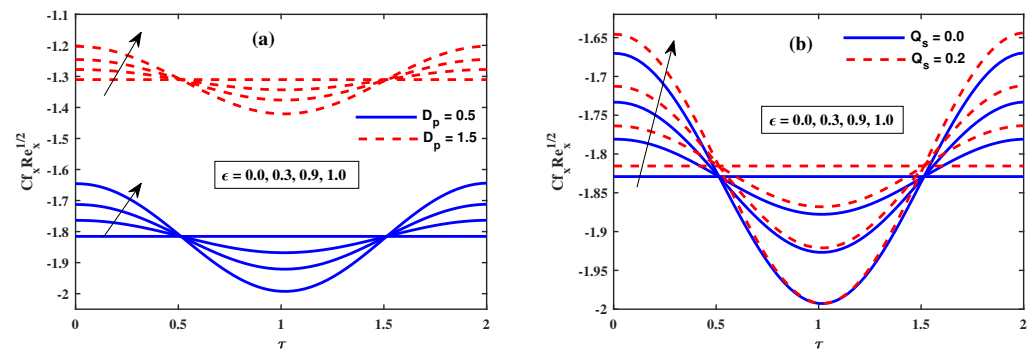
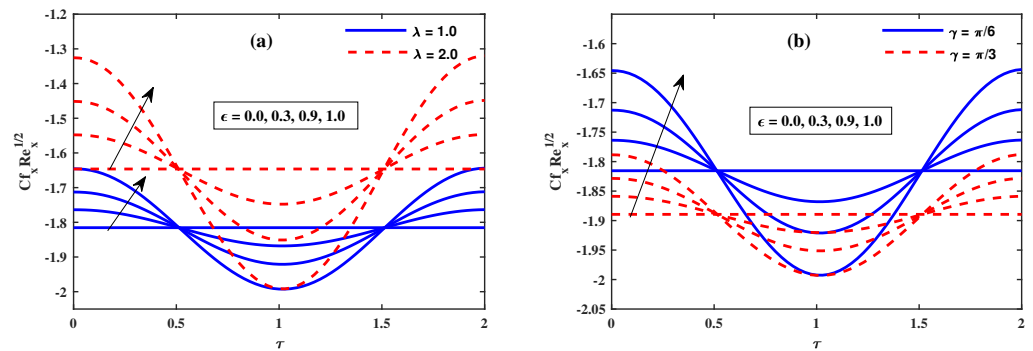
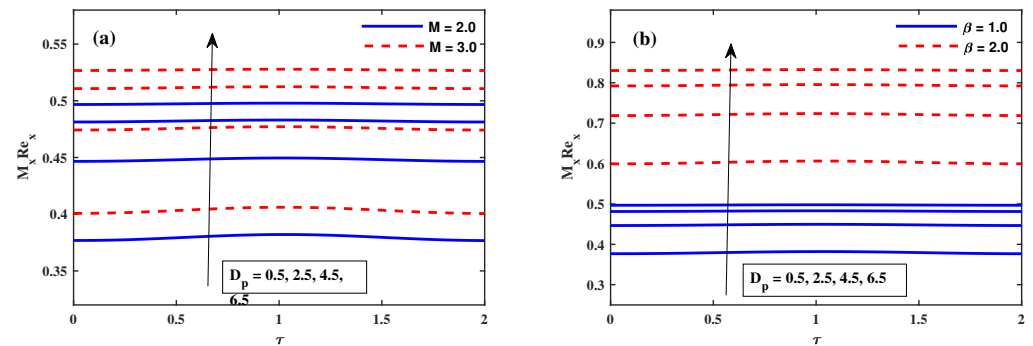


Figure 7. Fluctuation of  $Cf_x Re_x^{1/2}$  against  $\epsilon$  (amplitude), (a)  $D_p$  (nanoparticle radius), and (b)  $Q_s$  (heat source).



**Figure 8.** Fluctuation of  $Cf_x Re_x^{1/2}$  against  $\epsilon$  (amplitude), (a)  $\lambda$  (mixed convection parameter), and (b)  $\gamma$  (inclined angle).



**Figure 9.** Fluctuation of  $M_x Re_x$  (couple stress) against  $D_p$  (nanoparticle radius), (a)  $M$  (magnetic field), and (b)  $\beta$  (material parameter).

The implication of the radius  $D_p$  of nanoparticles on Nusselt number  $Nu_x Re_x^{1/2}$  is shown in Figure 10a,b. The observation was persuasive that the Nusselt number acquires a higher value against the increasing values of  $D_p$ . This remarkable impression of  $D_p$  on the Nusselt number of nanofluid against the incremental size of nanoentities is in conjunction with the findings of Arani et al. [53]. As discussed above, the temperature of the fluid is lowered against  $D_p$ ; hence, more heat transfer at the wall surface takes place. Further, it is seen that the Nusselt number remains almost uniform for all  $\tau$  ( $0 \leq \tau \leq 2$ ) for steady solution ( $\epsilon = 0$ ) and the stronger magnetic parameter  $M$  reduces  $Nu_x Re_x^{1/2}$ . The large values of  $M$  are related to higher Lorentz force, which resists the fluid flow and results in improved thermal conductivity. Since the fluid temperature is improved with growing values of magnetic field, the respective heat transfer rate at the sheet surface will be decreased. However, the larger values of the material parameter improved the modulated Nusselt number. Figures 11 and 12 are sketched to delineate the Nusselt number against  $\tau$  for various values of modulation amplitude  $\epsilon$  in collaboration with other parameters of interest. It is seen from Figure 11a that the larger-sized nanoparticles enhance  $Nu_x Re_x^{1/2}$ . This is an interesting finding to reveal the increasing/decreasing behavior of  $Nu_x Re_x^{1/2}$ , as influenced by the varying radius  $D_p$  in two situations, namely, the steady solution ( $\epsilon = 0$ ) in Figure 10 and with periodical gravity modulation ( $\epsilon > 0$ ) in Figure 11a. These results correspond to our fundamental aim of the study to analyze the role of increasing radius  $D_p$  for mixed convection related to microgravity modulated flow. Figure 11b shows that the oscillating Nusselt number recedes significantly against the improved strength of  $Q_s$  ( $Q_s > 0$ ). Figure 12a,b illustrates the oscillating Nusselt number with a variety of modulation amplitudes  $\epsilon$ . As expected, the larger  $\epsilon$  improves the amplitude of modulated heat transfer rate at the wall and exhibits greater deviation from its steady state mean value. Figure 12a also indicates that the growth of mixed convection parameter  $\lambda > 0$  enhances

the Nusselt number. In contrast, Figure 2b displays the declination of  $Nu_x Re_x^{1/2}$  against the increasing inclination of the sheet.

**Table 3.**  $F''(0)$  and  $H'(0)$  against  $M$  and  $\beta$  when  $\lambda = \Omega = \gamma = \epsilon = \Phi = 0.0, \chi_1 = 1.0$ .

$M$	$\beta$	Ali et al. [54]		Abdal et al. [19]		Present Results	
		$F''(0)$	$H'(0)$	$F''(0)$	$H'(0)$	$F''(0)$	$H'(0)$
0.0	0.2	-0.909698	0.094995	-0.909798	0.094895	-0.909841	0.095001
0.5	–	-1.114368	0.105085	-1.114378	0.105088	-1.114368	0.105094
1.0	–	-1.287147	0.112058	-1.287148	0.112048	-1.287114	0.112120
1.0	0.0	-1.414208	0.000000	-1.414228	0.000000	-1.414233	0.000001
–	0.5	-1.140781	0.211157	-1.140772	0.211165	-1.140730	0.211159
–	2.0	-0.769749	0.358659	-0.769755	0.358646	-0.769763	0.358608

**Table 4.**  $\theta'(0)$  via  $Pr$  when  $\lambda = \Omega = \gamma = \epsilon = Q_s = M = \beta = \Phi = 0.0, \chi_1 = 1.0$ .

$Pr$	Sharidan et al. [30]	Khan et al. [55]	Liaqat et al. [56]	Present Results
0.72	-0.8086	0.8088	0.80863	0.808633
1.0	-1.0000	1.0000	1.00001	1.000008
3.0	-1.9238	1.9237	1.92367	1.923676
10	-3.7225	3.7207	3.72067	3.720669

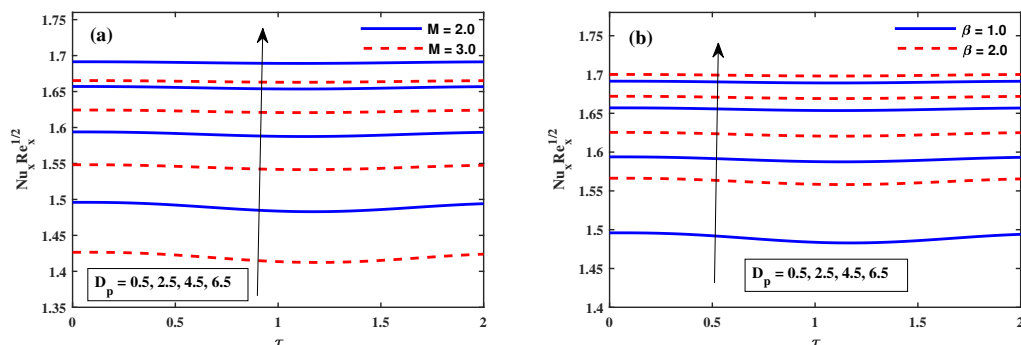


**Figure 10.** Fluctuation of  $Nu_x Re_x^{1/2}$  against  $D_p$  (nanoparticle radius), (a)  $M$  (magnetic field), and (b)  $\beta$  (material parameter).

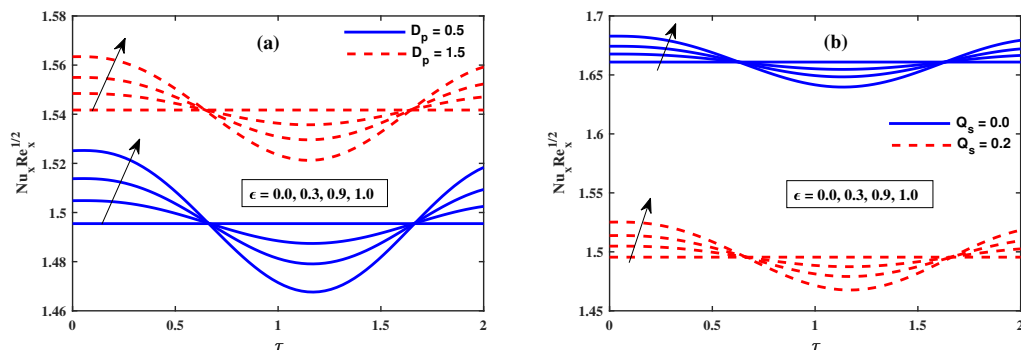


**Figure 11.** Fluctuation of  $Nu_x Re_x^{1/2}$  against  $\epsilon$  (amplitude), (a)  $D_p$  (nanoparticle radius), and (b)  $Q_s$  (heat source).

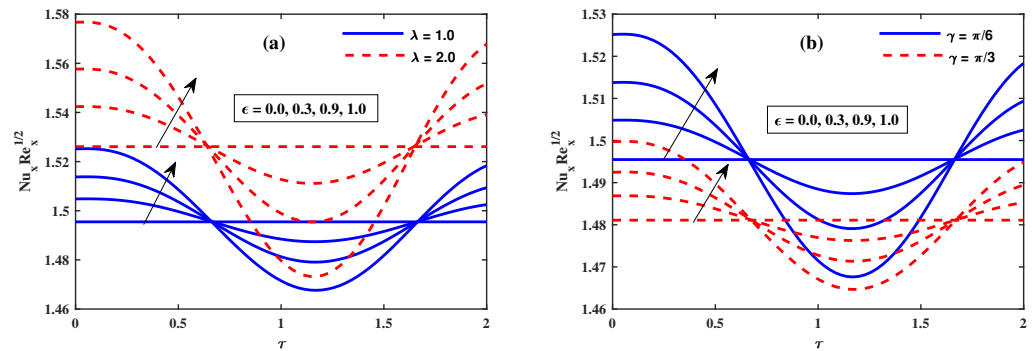


**Figure 12.** Fluctuation of  $Nu_x Re_x^{1/2}$  against  $\epsilon$  (amplitude), (a)  $\lambda$  (mixed convection parameter), and (b)  $\gamma$  (inclined angle).

**4. Conclusions**

With fixed inter-particle spacing, the variation of the radius of Copper nanoparticles is studied for microgravity-modulated mixed convection micropolar nanofluid flow because of an inclined sheet in the presence of heat source and magnetic field. By using FE simulation, the normalized microrotation  $H(\tau, \eta)$ , fluid velocity  $F'(\tau, \eta)$ , temperature, Nusselt number, decreased couple stress, and skin friction are examined and the crucial consequences are reported below:

1. The increment in the radius of nanoentities  $D_p$  augments the velocity  $F'(\tau, \eta)$ , and
  - reduces the temperature of Cu-nanofluids;
  - recedes the micromotion close the sheet’s boundary and twists to obtain rising values far off from the inclined sheet;
  - reduces the skin friction magnitude and enhances the Nusselt number  $Nu_x Re_x^{1/2}$  and couple stress.
2. The growing strength of frequency of oscillation and inclination angle leads to a decline in the values of reduced skin friction and heat transfer coefficient; however, an opposite trend is reported when the thermal buoyancy parameter is enhanced.
3. The stronger magnetic parameter  $M$  reduces the component of velocity  $F'(\tau, \eta)$ , and
  - Nusselt number ( $Nu_x Re_x^{1/2}$ ) attains lower values but skin friction coefficients gain larger values;
  - the rise of temperature  $\theta(\xi, \eta)$  is reported and exhibits the opposite trend for microrotation distribution.
4. The rising values of heat source, nanoparticles radius, and frequency of oscillation lead to a decrease in reduced skin friction and heat transfer coefficient, while an opposite trend is observed for Nusselt number against increasing radius.
5. Increase in the material parameter ( $\beta$ ), which is responsible for the increase in the velocity component  $F'(\tau, \eta)$ , and
  - temperature distribution diminishes but the microrotation profile attains higher values.
  - Nusselt number ( $Nu_x Re_x^{1/2}$ ), skin friction factor, and couple stress attain higher values.
6. The larger  $\epsilon$  improves the oscillating value of  $Cf_x Re_x^{1/2}$ , the amplitude of modulated heat transfer rate at the wall, and couple stress.

By this computational endeavor, we have successfully clarified the effect of nanoparticle radius on the non-Newtonian fluid (micropolar fluid) dynamics associated with microgravity (g-jitter). This research could be expanded for non-Newtonian fluids: viscoelastic Jeffrey’s nanofluid, Casson nanofluid, tangent hyperbolic, Maxwell nanofluid, and Oldroyd-B nanofluid.

**Author Contributions:** B.A.; Writing—review & editing, A.S.; Validation, M.M.A.; Writing—original draft, A.A.H.; Data curation, A.K.H.; Resources, and N.A.S.; supervision. All authors have read and agreed to the published version of the manuscript.

**Funding:** Princess Nourah bint Abdulrahman University Researchers Supporting Project number (PNURSP2023R132), Princess Nourah bint Abdulrahman University, Riyadh, Saudi Arabia.

**Institutional Review Board Statement:** Not applicable.

**Informed Consent Statement:** Not applicable.

**Data Availability Statement:** The numerical data used to support the findings of this study are included within the article.

**Conflicts of Interest:** The authors declare no conflict of interest.

## References

1. Khodadadi, H.; Toghraie, D.; Karimipour, A. Effects of nanoparticles to present a statistical model for the viscosity of MgO-Water nanofluid. *Powder Technol.* **2019**, *342*, 166–180. [[CrossRef](#)]
2. Ali, B.; Nie, Y.; Hussain, S.; Habib, D.; Abdal, S. Insight into the dynamics of fluid conveying tiny particles over a rotating surface subject to Cattaneo–Christov heat transfer, Coriolis force, and Arrhenius activation energy. *Comput. Math. Appl.* **2021**, *93*, 130–143. [[CrossRef](#)]
3. Wei, Y.; Rehman, S.U.; Fatima, N.; Ali, B.; Ali, L.; Chung, J.D.; Shah, N.A. Significance of dust particles, nanoparticles radius, coriolis and lorentz forces: The case of maxwell dusty fluid. *Nanomaterials* **2022**, *12*, 1512. [[CrossRef](#)] [[PubMed](#)]
4. Goodarzi, M.; Toghraie, D.; Reiszadeh, M.; Afrand, M. Experimental evaluation of dynamic viscosity of ZnO–MWCNTs/engine oil hybrid nanolubricant based on changes in temperature and concentration. *J. Therm. Anal. Calorim.* **2019**, *136*, 513–525. [[CrossRef](#)]
5. Zadeh, A.D.; Toghraie, D. Experimental investigation for developing a new model for the dynamic viscosity of silver/ethylene glycol nanofluid at different temperatures and solid volume fractions. *J. Therm. Anal. Calorim.* **2018**, *131*, 1449–1461. [[CrossRef](#)]
6. Hamid, M.; Usman, M.; Zubair, T.; Haq, R.U.; Wang, W. Shape effects of MoS<sub>2</sub> nanoparticles on rotating flow of nanofluid along a stretching surface with variable thermal conductivity: A Galerkin approach. *Int. J. Heat Mass Transf.* **2018**, *124*, 706–714. [[CrossRef](#)]
7. Yapici, K.; Osturk, O.; Uludag, Y. Dependency of nanofluid rheology on particle size and concentration of various metal oxide nanoparticles. *Braz. J. Chem. Eng.* **2018**, *35*, 575–586. [[CrossRef](#)]
8. Gajghate, S.S.; Bandurkar, A.V.; Das, S.; Saha, B.B.; Bhaumik, S. Effect of ZrO<sub>2</sub> nanoparticle deposited layer on Pool boiling heat transfer enhancement. *Heat Transf. Eng.* **2020**, *42*, 1184–1202. [[CrossRef](#)]
9. Shah, N.A.; Animasaun, I.; Chung, J.D.; Wakif, A.; Alao, F.; Raju, C. Significance of nanoparticle’s radius, heat flux due to concentration gradient, and mass flux due to temperature gradient: The case of Water conveying copper nanoparticles. *Sci. Rep.* **2021**, *11*, 1882. [[CrossRef](#)]
10. Ali, B.; Siddique, I.; Hussain, S.; Ali, L.; Baleanu, D. Boger nanofluid: Significance of Coriolis and Lorentz forces on dynamics of rotating fluid subject to suction/injection via finite element simulation. *Sci. Rep.* **2022**, *12*, 1612. [[CrossRef](#)]
11. Alhowaity, A.; Bilal, M.; Hamam, H.; Alqarni, M.; Mukdasai, K.; Ali, A. Non-Fourier energy transmission in power-law hybrid nanofluid flow over a moving sheet. *Sci. Rep.* **2022**, *12*, 10406. [[CrossRef](#)]
12. Nadeem, M.; Siddique, I.; Awrejcewicz, J.; Bilal, M. Numerical analysis of a second-grade fuzzy hybrid nanofluid flow and heat transfer over a permeable stretching/shrinking sheet. *Sci. Rep.* **2022**, *12*, 1631. [[CrossRef](#)]
13. Barnoon, P.; Toghraie, D.; Dehkordi, R.B.; Abed, H. MHD mixed convection and entropy generation in a lid-driven cavity with rotating cylinders filled by a nanofluid using two phase mixture model. *J. Magn. Magn. Mater.* **2019**, *483*, 224–248. [[CrossRef](#)]
14. Abdal, S.; Siddique, I.; Alrowaili, D.; Al-Mdallal, Q.; Hussain, S. Exploring the magnetohydrodynamic stretched flow of Williamson Maxwell nanofluid through porous matrix over a permeated sheet with bioconvection and activation energy. *Sci. Rep.* **2022**, *12*, 278. [[CrossRef](#)]
15. Eringen, A.C. Theory of micropolar elasticity. In *Microcontinuum Field Theories*; Springer: Berlin/Heidelberg, Germany, 1999; pp. 101–248.
16. Eringen, A.C. Theory of thermomicrofluids. *J. Math. Anal. Appl.* **1972**, *38*, 480–496. [[CrossRef](#)]
17. Willson, A. Boundary layers in micropolar liquids. *Math. Proc. Camb. Philos. Soc.* **1970**, *67*, 469–476. [[CrossRef](#)]
18. Shafie, S.; Amin, N.S.; Pop, I. G-Jitter free convection boundary layer flow of a micropolar fluid near a three-dimensional stagnation point of attachment. *Int. J. Fluid Mech. Res.* **2005**, *32*, 291–309. [[CrossRef](#)]
19. Abdal, S.; Ali, B.; Younas, S.; Ali, L.; Mariam, A. Thermo-Diffusion and Multislip Effects on MHD Mixed Convection Unsteady Flow of Micropolar Nanofluid over a Shrinking/Stretching Sheet with Radiation in the Presence of Heat Source. *Symmetry* **2020**, *12*, 49. [[CrossRef](#)]
20. Ali, B.; Raju, C.; Ali, L.; Hussain, S.; Kamran, T. G-Jitter impact on magnetohydrodynamic non-Newtonian fluid over an inclined surface: Finite element simulation. *Chin. J. Phys.* **2021**, *71*, 479–491. [[CrossRef](#)]

21. Pan, B.; Shang, D.; Li, B.; De Groh, H. Magnetic field effects on g-jitter induced flow and solute transport. *Int. J. Heat Mass Transf.* **2002**, *45*, 125–144. [[CrossRef](#)]
22. Ma, N.; Walker, J.S. Magnetic damping of buoyant convection during semiconductor crystal growth in microgravity: Spikes on residual acceleration. *Phys. Fluids* **1996**, *8*, 944–949. [[CrossRef](#)]
23. Li, K.; Li, B.; De Groh, H. Effect of magnetic field on g-jitter induced convection and solute striation during solidification in space. *Int. J. Heat Mass Transf.* **2003**, *46*, 4799–4811. [[CrossRef](#)]
24. Baumgartl, J.; Müller, G. The use of magnetic fields for damping the action of gravity fluctuations (g-jitter) during crystal growth under microgravity. *J. Cryst. Growth* **1996**, *169*, 582–586. [[CrossRef](#)]
25. Li, B. Stability of modulated-gravity-induced thermal convection in magnetic fields. *Phys. Rev. E* **2001**, *63*, 041508. [[CrossRef](#)] [[PubMed](#)]
26. Dou, X.; Chen, Z.; Zuo, P.; Cao, X.; Liu, J. Directional motion of the foam carrying oils driven by the magnetic field. *Sci. Rep.* **2021**, *11*, 21282. [[CrossRef](#)] [[PubMed](#)]
27. Li, B.Q. g-jitter induced free convection in a transverse magnetic field. *Int. J. Heat Mass Transf.* **1996**, *39*, 2853–2860. [[CrossRef](#)]
28. Rees, D.A.S.; Pop, I. The effect of large-amplitude g-jitter vertical free convection boundary-layer flow in porous media. *Int. J. Heat Mass Transf.* **2003**, *46*, 1097–1102. [[CrossRef](#)]
29. Siddheshwar, P.G.; Pranesh, S. Effect of temperature/gravity modulation on the onset of magneto-convection in weak electrically conducting fluids with internal angular momentum. *J. Magn. Magn. Mater.* **1999**, *192*, 159–176. [[CrossRef](#)]
30. Sharidan, S.; Amin, N.; Pop, I. g-jitter mixed convection adjacent to a vertical stretching sheet. *Microgravity-Sci. Technol.* **2006**, *18*, 5–14. [[CrossRef](#)]
31. Kiran, P. Throughflow and Gravity Modulation Effects on Heat Transport in a Porous Medium. *J. Appl. Fluid Mech.* **2016**, *9*, 1105–1113. [[CrossRef](#)]
32. Ashraf, M.A.; Peng, W.; Zare, Y.; Rhee, K.Y. Effects of size and aggregation/agglomeration of nanoparticles on the interfacial/interphase properties and tensile strength of polymer nanocomposites. *Nanoscale Res. Lett.* **2018**, *13*, 1–7. [[CrossRef](#)]
33. Vishal, C.C.; Kanala, R.K.; Raju, C.S.K.; Madathil, P.K.; Saha, P.; Rao, B.R.; Sriganesh, G.; Ramesh, K. Sub-micron sized metal oxides based organic thermic fluids with enhanced thermo-physical properties. *Appl. Therm. Eng.* **2019**, *163*, 114337. [[CrossRef](#)]
34. Ali, B.; Naqvi, R.A.; Mariam, A.; Ali, L.; Aldossary, O.M. Finite Element Study for Magneto-hydrodynamic (MHD) Tangent Hyperbolic Nanofluid Flow over a Faster/Slower Stretching Wedge with Activation Energy. *Mathematics* **2021**, *9*, 25. [[CrossRef](#)]
35. Khan, S.A.; Nie, Y.; Ali, B. Multiple slip effects on magnetohydrodynamic axisymmetric buoyant nanofluid flow above a stretching sheet with radiation and chemical reaction. *Symmetry* **2019**, *11*, 1171. [[CrossRef](#)]
36. Rawi, N.A.; Kasim, A.R.M.; Ali, A.; Isa, M.; Shafie, S. The effect of g-jitter on double diffusion by mixed convection past an inclined stretching sheet. *AIP Conf. Proc.* **2014**, *1605*, 392–397.
37. Rawi, N.A.; Zin, N.A.M.; Kasim, A.R.M.; Shafie, S. g-jitter induced MHD mixed convection flow of nanofluids past a vertical stretching sheet. *AIP Conf. Proc.* **2016**, *1750*, 030017.
38. Kumar, L. Finite element analysis of combined heat and mass transfer in hydromagnetic micropolar flow along a stretching sheet. *Comput. Mater. Sci.* **2009**, *46*, 841–848. [[CrossRef](#)]
39. Alanazi, M.M.; Hendi, A.A.; Ahammad, N.A.; Ali, B.; Majeed, S.; Shah, N.A. Significance of Ternary Hybrid Nanoparticles on the Dynamics of Nanofluids over a Stretched Surface Subject to Gravity Modulation. *Mathematics* **2023**, *11*, 809. [[CrossRef](#)]
40. Ali, B.; Naqvi, R.A.; Ali, L.; Abdal, S.; Hussain, S. A Comparative Description on Time-Dependent Rotating Magnetic Transport of a Water Base Liquid H<sub>2</sub>O With Hybrid Nano-materials Al<sub>2</sub>O<sub>3</sub>–Cu and Al<sub>2</sub>O<sub>3</sub>–TiO<sub>2</sub> Over an Extending Sheet Using Buongiorno Model: Finite Element Approach. *Chin. J. Phys.* **2021**, *70*, 125–139. [[CrossRef](#)]
41. Devi, S.S.U.; Devi, S.A. Numerical investigation of three-dimensional hybrid Cu–Al<sub>2</sub>O<sub>3</sub>/water nanofluid flow over a stretching sheet with effecting Lorentz force subject to Newtonian heating. *Can. J. Phys.* **2016**, *94*, 490–496. [[CrossRef](#)]
42. Graham, A.L. On the viscosity of suspensions of solid spheres. *Appl. Sci. Res.* **1981**, *37*, 275–286. [[CrossRef](#)]
43. Gosukonda, S.; Gorti, V.S.; Baluguri, S.B.; Sakam, S.R. Particle spacing and chemical reaction effects on convective heat transfer through a nano-fluid in cylindrical annulus. *Procedia Eng.* **2015**, *127*, 263–270. [[CrossRef](#)]
44. Ali, B.; Hussain, S.; Nie, Y.; Ali, L.; Hassan, S.U. Finite element simulation of bioconvection and cattaneo-Christov effects on micropolar based nanofluid flow over a vertically stretching sheet. *Chin. J. Phys.* **2020**, *68*, 654–670. [[CrossRef](#)]
45. Reddy, J.N. *Solutions Manual for an Introduction to the Finite Element Method*; McGraw-Hill: New York, NY, USA, 1993; p. 41.
46. Jyothi, K.; Reddy, P.S.; Reddy, M.S. Carreau nanofluid heat and mass transfer flow through wedge with slip conditions and nonlinear thermal radiation. *J. Braz. Soc. Mech. Sci. Eng.* **2019**, *41*, 415. [[CrossRef](#)]
47. Ali, B.; Pattnaik, P.; Naqvi, R.A.; Waqas, H.; Hussain, S. Brownian motion and thermophoresis effects on bioconvection of rotating Maxwell nanofluid over a Riga plate with Arrhenius activation energy and Cattaneo-Christov heat flux theory. *Therm. Sci. Eng. Prog.* **2021**, 100863. [[CrossRef](#)]
48. Ali, B.; Yu, X.; Sadiq, M.T.; Rehman, A.U.; Ali, L. A Finite Element Simulation of the Active and Passive Controls of the MHD Effect on an Axisymmetric Nanofluid Flow with Thermo-Diffusion over a Radially Stretched Sheet. *Processes* **2020**, *8*, 207. [[CrossRef](#)]
49. Namburu, P.; Kulkarni, D.; Dandekar, A.; Das, D. Experimental investigation of viscosity and specific heat of silicon dioxide nanofluids. *Micro Nano Lett.* **2007**, *2*, 67–71. [[CrossRef](#)]

50. Pastoriza-Gallego, M.J.; Lugo, L.; Legido, J.L.; Piñeiro, M.M. Thermal conductivity and viscosity measurements of ethylene glycol-based Al<sub>2</sub>O<sub>3</sub> nanofluids. *Nanoscale Res. Lett.* **2011**, *6*, 1–11. [[CrossRef](#)]
51. Vickers, N.J. Animal communication: When i'm calling you, will you answer too? *Curr. Biol.* **2017**, *27*, R713–R715. [[CrossRef](#)]
52. Esfe, M.H.; Saedodin, S.; Wongwises, S.; Toghraie, D. An experimental study on the effect of diameter on thermal conductivity and dynamic viscosity of Fe/water nanofluids. *J. Therm. Anal. Calorim.* **2015**, *119*, 1817–1824. [[CrossRef](#)]
53. Arani, A.A.; Amani, J. Experimental investigation of diameter effect on heat transfer performance and pressure drop of TiO<sub>2</sub>–water nanofluid. *Exp. Therm. Fluid Sci.* **2013**, *44*, 520–533. [[CrossRef](#)]
54. Ali, L.; Liu, X.; Ali, B.; Mujeed, S.; Abdal, S. Finite Element Simulation of Multi-Slip Effects on Unsteady MHD Bioconvective Micropolar nanofluid Flow Over a Sheet with Solutal and Thermal Convective Boundary Conditions. *Coatings* **2019**, *9*, 842. [[CrossRef](#)]
55. Khan, S.A.; Nie, Y.; Ali, B. Multiple slip effects on MHD unsteady viscoelastic nano-fluid flow over a permeable stretching sheet with radiation using the finite element method. *SN Appl. Sci.* **2020**, *2*, 66. [[CrossRef](#)]
56. Ali, L.; Liu, X.; Ali, B.; Mujeed, S.; Abdal, S. Finite Element Analysis of Thermo-Diffusion and Multi-Slip Effects on MHD Unsteady Flow of Casson Nano-Fluid over a Shrinking/Stretching Sheet with Radiation and Heat Source. *Appl. Sci.* **2019**, *9*, 5217. [[CrossRef](#)]

**Disclaimer/Publisher's Note:** The statements, opinions and data contained in all publications are solely those of the individual author(s) and contributor(s) and not of MDPI and/or the editor(s). MDPI and/or the editor(s) disclaim responsibility for any injury to people or property resulting from any ideas, methods, instructions or products referred to in the content.